

Seismic fragility of a typical bridge using extrapolated experimental damage limit states

Yang Liu^{1a}, Fabrizio Paolacci^{2b} and Da-Gang Lu^{*1}

¹School of Civil Engineering, Harbin Institute of Technology, Harbin 150090, P.R. China

²Department of Engineering, Roma Tre University, Rome, Italy

(Received October 9, 2017, Revised January 5, 2018, Accepted January 16, 2018)

Abstract. This paper improves seismic fragility of a typical steel-concrete composite bridge with the deck-to-pier connection joint configuration at the concrete crossbeam (CCB). Based on the quasi-static test on a typical steel-concrete composite bridge model under the SEQBRI project, the damage states for both of the critical components, the CCB and the pier, are identified. The finite element model is developed, and calibrated using the experimental data to model the damage states of the CCB and the bridge pier as observed from the experiment of the test specimen. Then the component fragility curves for both of the CCB and the pier are derived and combined to develop the system fragility curves of the bridge. The uncertainty associated with the mean system fragility has been discussed and quantified. The study reveals that the CCB is more vulnerable than the pier for certain damage states and the typical steel-concrete composite bridge with CCB exhibits desirable seismic performance.

Keywords: seismic fragility; steel-concrete composite bridge; quasi-static test; concrete crossbeam; damage state

1. Introduction

Nowadays, the short-to-medium span steel-concrete composite bridges have been extensively used in the highway networks, especially in the North America and European continent, due to the advantages of (I) convenient construction and minor effects on the traffic under bridges; (II) small beam depth and low self-weight; and (III) excellent structural integrity under earthquakes (Paolacci *et al.* 2014). In the regions with high seismic hazard, severe damage or collapse of these overpass bridges by earthquakes can cause blockages of the right-underneath highway, so that the post-seismic rescue and emergency disaster mitigation strategies can be significantly impacted. This necessitates the study on the seismic performance of the typical composite bridges for the planning of post-disaster rescue and decision-making. In addition, comparing with many investigations associated with the bridge piers, the experimental investigations on the critical component of the composite bridge, i.e., the Concrete Crossbeam (CCB), have been still limited. The inadequate experiment data of the CCB used in developing the component fragility of the composite bridge can cause un-negligible errors in the fragility analysis. Therefore, this paper will focus on the development of fragility curves of the CCB extrapolated from the experimental test, and then carry out seismic

fragility analysis for the typical steel-concrete composite bridge.

The framework for performance-based earthquake engineering have been proposed for many years and a lot of applications had been performed on the fragility analysis of bridges under this framework (Muntasir Billah and Shahria Alam 2015). Given that the seismic fragility is defined as the failure probability of a structure reaching or exceeding certain damage states at a given level of seismic intensity measure, determination of the threshold of damage state of the structure (i.e., the limit states) is an essential subject (Sengupta and Li 2013, 2014, Stefanidou and Kappos 2017).

Limit states are commonly identified based on the experimental data or can be estimated through the numerical analyses or hybrid methods using both of experimental and numerical techniques (Muntasir Billah and Shahria Alam 2015). The analytical approach was used in numerous works and has the advantages of considering the various types of uncertainties; However, it is difficult to select a proper analysis technique and define the reasonable limit states (Padgett and Desroches 2008, Baker 2013). On the contrary, the experimental approach allows a direct observation of the limit states of structures (Banerjee and Chi 2013, Han *et al.* 2014). The hybrid approach can result in large dispersion on probabilistic models (Frankie 2013). In this paper, both experimental and analytical approaches are adopted to identify the limit states of the CCB and the pier of the composite bridge.

The quasi-static test on the deck-to-pier joint with the CCB has been carried out under the SEQBRI project (Paolacci *et al.* 2016). A novel configuration of the CCB was proposed to improve the seismic performance of conventional short-to-medium span steel-concrete composite bridges (Paolacci *et al.* 2016). The reference

*Corresponding author, Professor
E-mail: ludagang@hit.edu.cn

^aPh.D. Student
E-mail: liuyang6886@163.com

^bAssistant Professor
E-mail: fabrizio.paolacci@uniroma3.it

bridge with two spans studied in this project is selected. The finite element (FE) model is developed, and calibrated using the experimental data, to model the damage states of the CCB and bridge pier as observed from the experiment of the test specimen. For the seismic damage data of the bridge piers, the experimental and analytical limit states are obtained based on the existing literature (Berry and Eberhard 2003, Stefanidou and Kappos 2017).

To account for the variabilities of earthquakes, both near-fault and far-field ground motions are selected from the NGA-West2 database (2017). To select the appropriate intensity measures, the sufficiency and efficiency of four intensity measures are evaluated. The 3-D FE model of the bridge is developed and calibrated by the experimental data. The cloud approach is utilized to establish the probabilistic seismic demand models with the peak ground acceleration (PGA). By using the limit states identified and the demand data simulated, the component fragility curves of the CCB and the pier are developed, respectively. Then the system fragility curves are derived by combining the component fragility curves to assess the fragility of the CCB and the composite bridge.

2. Methodology of seismic fragility analysis using analytical and experimental damage states

2.1 Fragility function

The seismic fragility can be expressed as the probability of the seismic demand (D) exceeding the seismic capacity (C) at the component or system level, conditioned on a given level of intensity measure IM (Lu *et al.* 2014). Assuming that random variables of both the demand (D) and the capacity (C) follow the lognormal distribution, the fragility can be expressed in a closed form as (Cornell *et al.* 2002)

$$P(D \geq C | IM) = \Phi \left[\frac{\ln(m_D) - \ln(m_C)}{\sqrt{\beta_{D|IM}^2 + \beta_C^2}} \right] \quad (1)$$

where m_D and $\beta_{D|IM}$ are the median and the dispersion of the seismic demand, respectively, and can be calculated through the procedure of probabilistic seismic demand analysis (PSDA); m_C and β_C are the median and dispersion of the capacity, respectively, and can be generally determined by damage analysis using the experimental or/and analytical approaches; $\Phi(\cdot)$ is the cumulative distribution function of the standard normal distribution.

The purpose of PSDA is to establish a probabilistic seismic demand model (PSDM) with a probabilistic relation model between the engineering demand parameters (EDPs) and IMs (Tondini and Stojadinovic 2012). In this paper, the PSDM of the bridge is developed using the Cloud Analysis method, by implementing the non-linear dynamic analyses through the linearly regressed probabilistic model. This model can be expressed as follows (Cornell *et al.* 2002)

$$m_D = E[D | IM = x] = ax^b \quad (2)$$

$$\beta_{D|IM} = \sqrt{\frac{\sum_{i=1}^N \ln(D_i) - \ln(m_D)^2}{N - 2}} \quad (3)$$

in which a and b are regression parameters, $E(\cdot)$ is the expected value of the demand, N is the number of nonlinear time-history analyses and D_i is the structural response in the i -th analyses.

2.2 Damage analysis and limit states

Damage analysis of structural components is to identify structural limit states and establish the probabilistic relation between EDPs and damage measures (DMs). Data of structural damage (under different damage extents) for a given EDP can be obtained by either experimental or analytical approaches. Based on the damage data, the parameters of the capacity, m_C and β_C , can be estimated by the following expressions (Ibarra 2005)

$$m_C = \exp\left(\frac{1}{N} \sum_{i=1}^N \ln(D_i)\right) \quad (4)$$

$$\beta_C = \sqrt{\frac{\sum_{i=1}^N \ln(D_i) - \ln(m_C)^2}{N - 1}} \quad (5)$$

where N is the number of specimens (or models), D_i is the value of EDP at which the damage corresponding to the limit state observed in the i -th specimen (or model). Unfortunately, the number of available specimens is often limited (e.g., 25 is recommended by Porter *et al.* (2007)), and the mean of EDP is often used to approximate the median of the capacity, whereas the dispersion of the capacity is calculated using the analytical approaches. To achieve for a comprehensive investigation on the seismic damages of the typical composite bridge, both experimental and analytical approaches are utilized in the present study.

3. Damage limit states of CCB and bridge piers

3.1 Damage limit states of CCB

3.1.1 Description of the prototype bridge with CCB

Details of the novel configuration of the CCB in a typical composite bridge, as proposed by Paolacci *et al.* (2016), are shown in Fig. 1. The concept of CCB is to transfer the loading from the composite girder to the CCB through contact and dedicated groups of Nelson studs. The tensile force at the top flange is transferred gradually to the longitudinal reinforcement (or reversely a potential compression force to the concrete slab) through a group of vertical studs, which are welded to the top flange of the steel girder on the left and right sides the CCB component. The top flange of the steel girder was trimmed (terminated) at the left and right side of the CCB zone. The shear force from the steel girder is transferred to the CCB through a group of horizontal studs (transversally placed at the sides of the girder's web), forming part of the CCB component. This group of studs is subjected only to the pure shear. The



Fig. 1 Pier-to-deck connection joint (CCB)

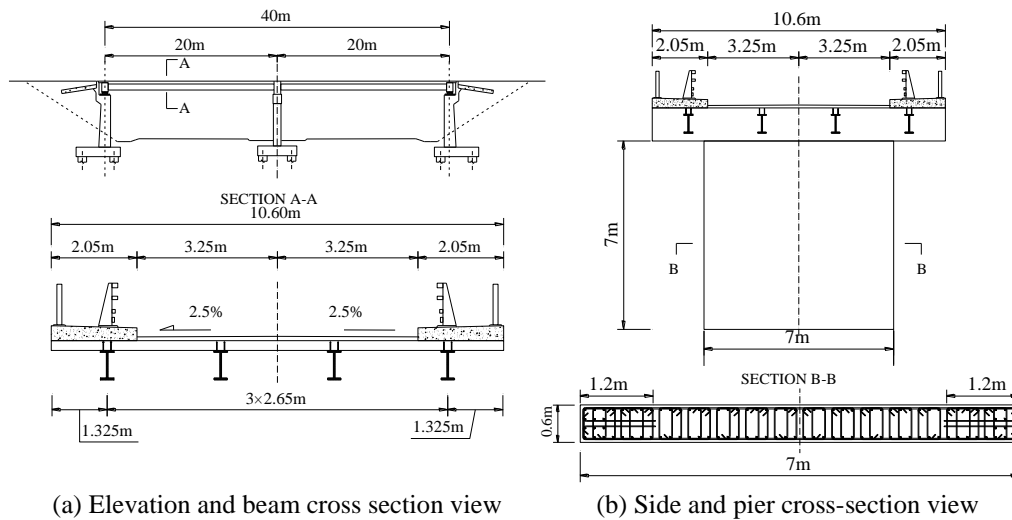


Fig. 2 The elevation and cross-section of the bridge

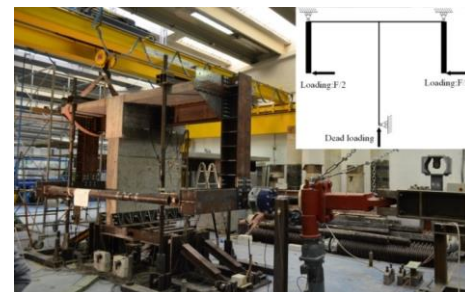
significant tensile force at the bottom flange of the CCB zone is achieved by the pre-stressed bars.

The prototype bridge is a typical short span overpass with two lanes (as shown in Fig. 2) and was investigated under the European Project SEQBRI (Paolacci *et al.* 2016). The bridge has two spans of 20.0 m each and the roadway width of 10.6 m (including a 6.5 m wide carriageway and two sidewalks of 2.05 m wide each). Four HE600B steel girders with a steel grade of S460 are used. These steel girders have a spacing of 2.65 m and have no transverse bracings. The thickness of the concrete slab is 25 cm. The steel girders are monolithically connected to the pier through a reinforced CCB with 0.9 m wide, whereas they are simply supported on normal (low) damping bearings at the abutment through an additional CCB.

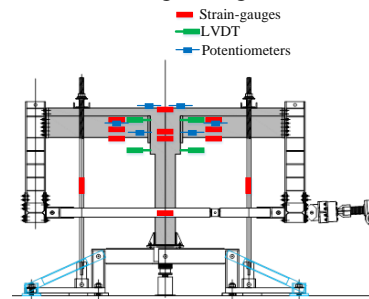
The wall-type pier has a height of 7.0 m, a thickness of 0.6 m and width of 7.0 m, as shown in Fig. 2. The soil beneath the foundation is assumed to be type B in accordance with EN1998 (CEN 2005) and the soil-structure interaction effect is neglected in this test.

3.1.2 Description of the quasi-static test of the specimen

Since CCB is one of the critical components for the composite bridge, four scaled specimens of the pier-to-deck connection were tested to investigate the mechanical behaviors and identify the critical damage states of the



(a) Testing configuration



(b) Measurement scheme

Fig. 3 Experimental setup under the longitudinal loading

connection (Paolacci *et al.* 2016). Quasi-static tests of the specimens under the longitudinal loading were performed at the laboratory of Roma Tre University.

The test specimen was fabricated with a scale ratio of 1/2 from its prototype to fit the laboratory test constraints. Fig. 3(a) presents the test configurations and experimental setup in the longitudinal direction. The specimens for the longitudinal tests are made of a single IPE330/S460 steel girder with the tributary concrete slab and portion of the pier made of concrete C35/45. The slab is 1.325 m wide, 12.5 cm thick and 3.5 m long. The pier is 2.0 m long and 30 cm thick. All the girders are fabricated to be 50 cm longer than the required to simulate the realistic boundary conditions in the test.

The layout of the measurement setup is shown in Fig. 3(b). The horizontal actuator is linked to the steel frame on the right side. The strain-gauges, linear variable differential transformer (LVDTs), and potentiometers are arranged to, respectively, measure the responses of the CCB and the portion of the composite beam.

Four specimens having the CCB configuration in Section 3.1.1 were constructed in the laboratory. Three of them were tested under the longitudinal loading and one was tested under the monotonic vertical loading. In the longitudinal loading test, both monotonic and cyclic loading methods are adopted. The monotonic test specimen (denoted as D2C3M) was tested to obtain the skeleton curve (i.e., the force and displacement at yielding and collapse conditions) as well as the mechanism of collapse in the CCB. After getting the yielding displacement, the cyclic loading amplitude was determined based on the ECCS (1986). Then the cyclic test specimens (denoted as D2C1C and D2C4C) were tested. In this paper, only the test results of specimens D2C3M, D2C1C, and D2C4C are presented and seismic fragility assessment of the prototype bridge under the longitudinal loading is conducted.

3.1.3 Extrapolation of damage limit states using the test results

As discussed in Section 2.1, damage analysis is one of the key steps within the PBEE framework to build the relationship between the structural response (EDPs) and physical damage (capacity) at the component or system levels. The progressive damage states for the repair cost estimation is provided by the damage analysis, while damage measures (DMs) are commonly used to define the damage states (Tubaldi *et al.* 2010).

Damage analysis of the CCB is performed based on the experimental data. The relative joint rotation θ between the end plate of steel girder and the CCB, as shown in Fig. 4, is selected as the EDP for the CCB. The corresponding DMs are selected as the yielding and the ultimate rotations of the CCB.

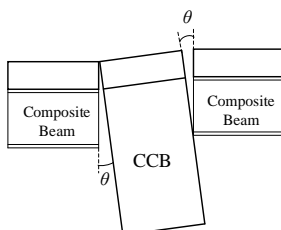


Fig. 4 The relative rotation of the CCB

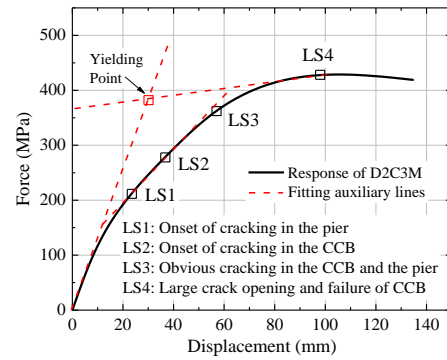
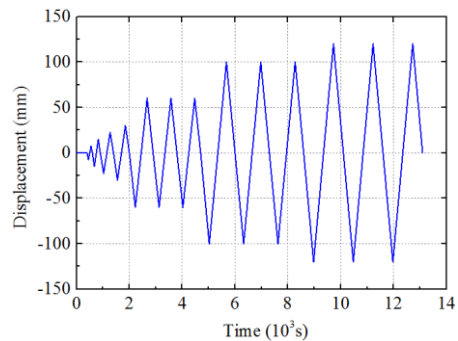
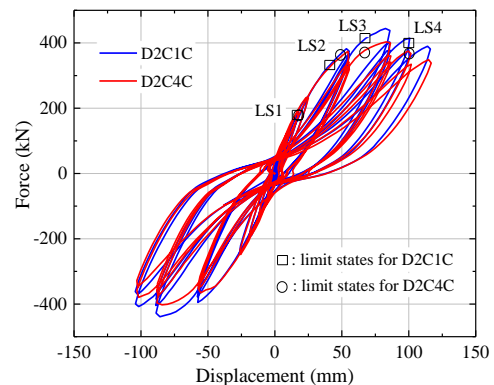


Fig. 5 Force vs. displacement response of D2C3M and limit states under monotonic loading



(a) The test load protocol



(b) Cyclic responses and limit states

Fig. 6 Cyclic loading protocol and limit states on cyclic responses of D2C1C and D2C4C

In the first phase, the monotonic test was performed on the specimen of D2C3M. The vertical load was imposed through the jack at the bottom of the middle pier. Fig. 5 shows the monotonic response and damage limit states for the D2C3M. Four sequential damage limit states are identified during the test process. This test reveals the damage involvement of the CCB component as both the lateral displacement and the force increase. Meanwhile, determination of the yielding displacement and force is based on the recommended procedure by Bursi *et al.* (2002), which utilizes the multi-linear curves to fit and approximate the test response of a specimen. According to this procedure, the yielding point was determined for specimen D2C3M with a relative displacement of 30 mm, as shown in Fig. 5.

Table 1 Limit states and EDPs for CCB under test

| LS for CCB | DMs | EDPs | m_c (mrad) | β_c |
|-------------------|-------------------|------------------------------|--------------|-----------|
| LS _{ce1} | Yielding rotation | Relative rotation of the CCB | 0.3 | 0.25 |
| LS _{ce2} | Ultimate rotation | Relative rotation of the CCB | 19 | 0.47 |

The yielding displacement identified from the response of D2C3M was used to calibrate the displacement history protocol for the cyclic test. The details of the imposed cyclic loading protocol are shown in Fig. 6(a). The cyclic tests on the specimens of D2C1C and D2C4C are conducted with the same loading rule and the same test setup. The force-displacement curves for the specimens D2C1C and D2C4C are presented in Fig. 6(b). It is observed from Fig. 6 that the cyclic responses of these two specimens are similar. The damage limit states for both D2C1C and D2C4C are identified following the similar phenomenon observed from the specimen D2C3M under the monotonic test. In addition, it was observed from the test that, the degradation of the hysteretic cycle occurred at a displacement of 60 mm is mainly due to the minor concrete cracking and steel yielding, along with the minor sliding occurred at the foundation base of the specimen.

According to the experimental results of relative rotations of the CCB, the maximum absolute value of rotations on the left and the right sides of the CCB under the same limit state condition is selected. Table 1 presents the selected DMs along with the mean values of the corresponding EDP for the CCB. Although three specimens (two under cyclic loading and one under monotonic loading) were tested under the longitudinal loading, the standard deviations for the limit states are assumed as the variation of the capacity calculated from the experimental test (shown in Table 1). In order to get more reliable results on the variation, the refined FE model is used to quantify the uncertainties in the following Section 3.1.4.

3.1.4 The FE model of the specimen and analytical damage limit states

A 2-D FE model of the testing specimen is built on the OpenSees platform (Mazzoni *et al.* 2006) and the model configuration is presented in Fig. 7. The nonlinear fiber beam elements are used to model the composite section with the steel girder and the tributary concrete slab, as shown in Fig. 8. The Menegotto-Pinto model is used as the constitutive model of steel girders and slab reinforcement, whereas the Kent-Park model is used as the constitutive model for the concrete. For steel material, the modulus of elasticity E_0 is 192 GPa for the flange, 204 GPa for the web, and 198 GPa for steel bars, along with the yield strength f_y of 522 MPa, 538 MPa, and 532 MPa, respectively. For concrete material, the compressive ultimate strength f_{cu} is 28 MPa with the corresponding strain ϵ_{cu} of 0.006. The compressive strength f_{c0} is given in Table 2 with the corresponding strain ϵ_{c0} of 0.002. The nonlinear beam elements are also adopted to model the pier with the fiber elements.

The nonlinear links with elastoplastic behavior are used

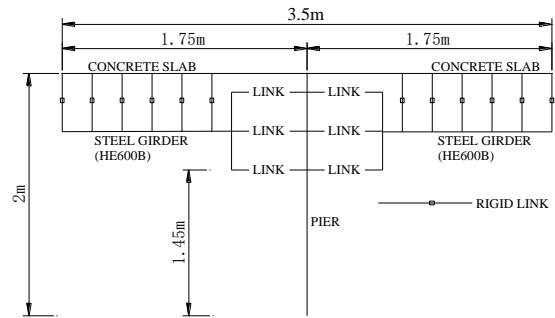


Fig. 7 Elevation view of the FE model of the test composite bridge specimen with CCB

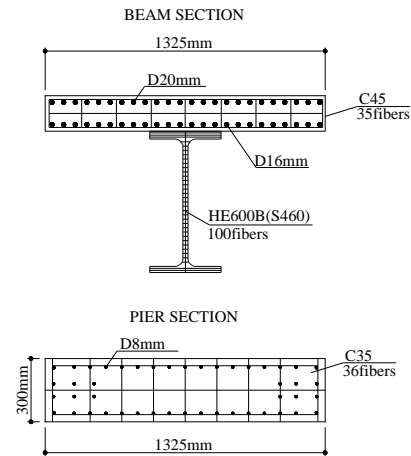


Fig. 8 Fiber sections of the composite beam

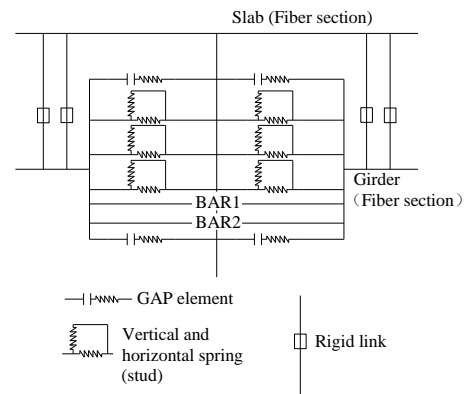


Fig. 9 2-D component-based model of the CCB joint

to model the vertical shear studs connecting the steel girders to the slab as well as the shear studs within the CCB. The strength of the shear studs has been evaluated in accordance with CEN (2006). The stiffness has been evaluated by means of the experimental load-slip curves defined by Gattesco and Giuriani (1996). The horizontal elastoplastic links are also used to simulate the shear studs along the deck, whereas the degree-of-freedom in the vertical direction and the rotation are constrained by the rigid links between girders and slab.

Fig. 9 shows the details of the 2-D FE model for the concrete crossbeam. Rigid links are used to model the vertical head plate which is welded on the steel girders and directly in contact with the transverse concrete beam.

Table 2 Probability distribution models and parameters for the random variables

| Random variables | Probability distribution model | Mean | COV |
|--|--------------------------------|-------|------|
| Compressive strength of concrete (MPa) | Normal | 34.5 | 0.18 |
| Ratio of thickness and width of pier cross section | Uniform | 0.226 | 0.03 |
| Ratio of thickness and width of slab cross section | Uniform | 0.094 | 0.02 |

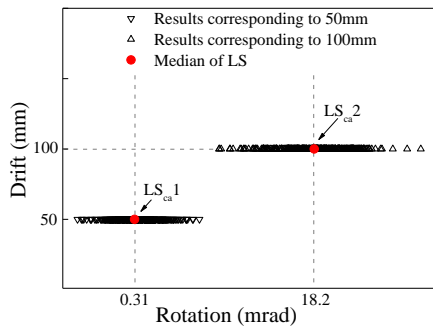


Fig. 10 Identification of the analytical limit states for CCB

Different nonlinear links modeling the behavior of the horizontal shear headed studs within the joint are connected to these rigid links according to the CCB configuration of Fig. 1. To simulate the constraint in compression due to the presence of the CCB, gap elements are adopted at both left and right sides of the CCB joint at two different heights, as shown in Fig. 9. A simplified procedure for evaluating the stiffness of the gap elements is performed, assuming that the compression force transferred by the girder will exert uniformly on the contact area of the vertical head plate. Two groups of the prestressing bars at the bottom area of the CCB are modeled by two elastic truss elements.

In the probabilistic modeling of the composite bridge with CCB component, a total of three parameters, including the compressive strength of concrete and the geometrical errors in concrete pier and slab, are considered as the random variables. The probability distribution function and the parameters for the selected random variables are presented in Table 2 (Nielson 2005).

Latin hypercube sampling (LHS) technique (Iman 2008) is employed to generate samples of the CCB FE models. A total of 1000 samples for each random variable is generated to obtain a total of 1000 different numerical models. According to experimental tests of CCB, the cyclic displacement histories with amplitudes ranging from 30 mm to 120 mm have been used for the nonlinear static simulations. The horizontal drift of 50 mm and 100 mm, corresponding to the experimental yielding and ultimate limit states of the CCB, are adopted into the FE models. It should be noted that the conditions with a displacement of 50 mm and 100 mm represent the yielding and ultimate conditions of the CCB component only. During the test, both the rotation and cracking occurred on the CCB component were observed and identified with different damage states, and the longitudinal displacement associated with each damage state is defined as the limit states. The

Table 3 Limit states and EDPs for CCB according to numerical simulation

| LS for CCB | Damage measure | Engineering demand parameter | m_c (mrad) | β_c |
|-------------------|-------------------|------------------------------|--------------|-----------|
| LS _{ca1} | Yielding rotation | Relative rotation of the CCB | 0.31 | 0.33 |
| LS _{ca2} | Ultimate rotation | Relative rotation of the CCB | 18.2 | 0.57 |

Table 4 Limit states and EDPs for bridge pier based on experimental test (Berry and Eberhard 2003)

| LS for pier | Damage measure | Engineering demand parameter | m_c (%) | β_c |
|-------------------|---------------------------------------|------------------------------|-----------|-----------|
| LS _{pe1} | Concrete cover spalling | Drift ratio | 1.2 | 0.33 |
| LS _{pe2} | Longitudinal reinforcing bar buckling | Drift ratio | 3.8 | 0.40 |
| LS _{pe3} | Longitudinal reinforcing bar fracture | Drift ratio | 4.4 | 0.45 |

numerical responses for the rotation of the CCB are presented in Fig. 10 under both the yielding and ultimate damage states. The median and dispersion of capacity of CCB are estimated based on Eqs. (4)-(5), and are reported in Table 3. Comparing the limit states of Table 1, the relative errors between the analytical and the experimental results are minor. It is worth mentioning that the ultimate capacity of the CCB estimated by the analytical model is smaller than that from the test. Therefore, conservative assessment results of the bridge can be obtained based on the analytical ultimate capacity results and they are used in this paper for seismic fragility analysis.

3.2 Damage limit states of the bridge pier

Bridge piers can experience various extents of seismic damages varying from the concrete cover spalling to the buckling and fracture of longitudinal reinforcement bar (Berry and Eberhard 2003). Concrete cover spalling normally indicates an initial damage state that may cause a potential short-term loss of serviceability along with a significant repair cost. While the buckling or fracture of the longitudinal reinforcement implies the structural inadequacy (i.e., safety concerns) issue that partial replacement of the structure and long-term recovery are required.

In this paper, the drift ratio is selected as the EDP corresponding to the DS of the pier. The empirical equations on the damage states (DS) proposed in Berry and Eberhard (2003) have been used to estimate the deformations of bridge pier under each damage level. The model is calibrated using a series of existing experimental tests from the UW-PEER reinforced concrete column performance database. The results are reported in Table 4.

The damage states for wall type pier analyzed by Stefanidou and Kappos (2017) are adopted. The median and the dispersion of component capacities are summarized in Table 5. A comparison with the values of Table 4 shows that the median values of the damage states corresponding to concrete cover spalling and buckling of longitudinal reinforcement are more dispersed.

Table 5 Limit states and EDP for piers based on the analytical model (Stefanidou and Kappos 2017)

| LS for pier | Damage measure | Engineering demand parameter | m_c (%) | β_c |
|-------------------|--|------------------------------|-----------|-----------|
| LS _{pa1} | Barely visible cracks | Drift ratio | 0.36 | 0.488 |
| LS _{pa2} | Spalling of cover concrete | Drift ratio | 0.72 | 0.542 |
| LS _{pa3} | Buckling of longitudinal reinforcement | Drift ratio | 1.87 | 0.538 |
| LS _{pa4} | Loss of load-carrying capacity | Drift ratio | 3.30 | 0.605 |

It should be noted that the common wall-type pier was designed in accordance with the EN1998 (CEN 2005) and the design reinforcement detail of the pier is shown in Fig. 2.

4. Probabilistic seismic demand analysis

4.1 Selection of input ground motions

Based on the PEER strong ground motion database, a total of 60 near-fault (NF) pulse-like ground motions and 60 far-field (FF) ground motions are selected. The NF earthquakes with moment magnitudes (M_w) greater than 6.0 and site-to-source distances (R) less than 20 km are selected (Liu *et al.* 2015, Han *et al.* 2017). In addition, the NF earthquakes with the ratio of peak ground velocity (PGV) and peak ground acceleration (PGA) being greater than 0.2 are included (Liu *et al.* 2016). The FF ground motions are selected to match both PGA and M_w of the NF records but with $R > 20$ km. The identification approach on the NF pulse-like ground motions by Zhai *et al.* (2013) is used to quantify the energy of strong velocity pulse. The detail of the selected ground motions is presented in Appendix A.

The selection of appropriate IMs is essential in the probabilistic demand analysis and fragility curves development. The efficiency and sufficiency criteria on selecting IMs presented in Luco and Cornell (2007) is used. The efficiency of an IM can be quantified through the dispersion of demand β_d and more efficient IMs result in a smaller variability of the structural response. The sufficiency of an IM can be quantified by statistical significance test of the linear regression of the logarithmic residual of demand ($\ln(\varepsilon)$) versus M or $\ln(R)$. The spectral acceleration $S_a(T_1)$ (abbreviated as S_a) is a commonly used IM; however, PGA has been widely used due to the higher efficiency (Padgett and Desroches 2008). For NF ground motions, PGA has also been recommended for fragility analysis of bridges (Billah *et al.* 2012); however, the largest value of PGA does not correlate well with the most severe damage of the structures and alternative IMs such as the Peak Ground Velocity (PGV) and displacement (PGD) are also recommended (Luco and Cornell 2007). In this paper, a total of four IMs, including S_a , PGA , PGV , and PGD , is evaluated to determine the most appropriate IM that is used in the fragility analysis of the composite bridge.

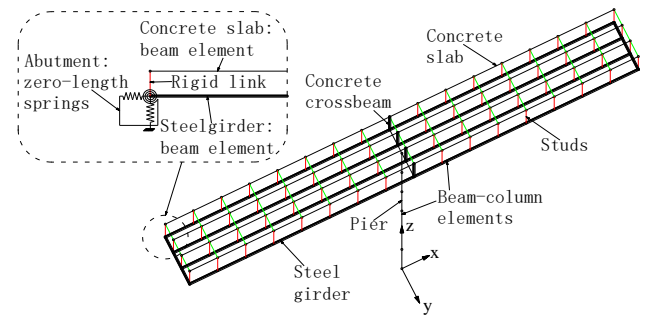


Fig. 11 3-D FE model of the prototype bridge

Table 6 Probability distribution models of the random variables

| Random variables(Unit) | Distribution | Mean | COV |
|--|--------------|-------|------|
| Compressive strength of concrete (MPa) | Normal | 34.5 | 0.18 |
| Yield strength of steel bar (MPa) | Lognormal | 6.13 | 0.08 |
| Ultimate concrete strain (%) | Normal | 0.99 | 0.36 |
| Damping ratio | Normal | 0.045 | 0.28 |

4.2 Probabilistic seismic demand model

Based on the calibrated FE model of the specimen, the 3-D FE model of the prototype bridge is developed on the platform of OpenSees (Mazzoni *et al.* 2006). The modeling of CCB component in the 3-D FE model is similar to those presented in Section 3.1.4. The superstructure of the bridge is built by using the horizontal link elements to connect four single beam models. Fig. 11 presents the 3-D FE model of the prototype bridge.

A total of four parameters, namely the yield strength of reinforcement bar, the compressive strength of concrete, the ultimate concrete strain and the damping ratio, is assumed as the random variables with probability distribution models in Table 6 (Celik and Ellingwood 2010). The ground motions selected in Appendix A are used to consider the record-to-record variability of the input earthquakes.

A total of 240 samples of bridge-earthquake models were generated based on the LHS technique (Iman 2008). The nonlinear time-history response analysis is performed to calculate structural responses for each sample of the bridge-earthquake model. The linear regression analysis is performed to calculate the parameters of the demand model (m_d and β_d) (Muntasir Billah and Shahria Alam 2015).

The dispersion values of the demand are given in Table 7 for the four IMs selected in Section 4.1. The statistical significance test of the linear regression analysis between the logarithmic residual of demand $\ln(\varepsilon)$ and versus M or $\ln(R)$ is also performed along with the p-values listed in Table 7. As seen from Table 7, the p-value corresponding to PGV and PGD are less than 0.05 (which is the commonly used statistical threshold), indicating that they are lack of sufficiency for the probabilistic demand analysis. The PGA tends to be a more efficient IM than S_a based on the lower dispersion results of demand in Table 7 (except for those associated with the relative rotation of CCB under far-field ground motions with minor difference). Therefore, the PGA is selected as the IM in the following fragility analysis.

Table 7 Dispersion of demand and p -value for different IMs

| IM | NF ground motions | | | | | | FF ground motions | | | | | |
|-------|-------------------|------------|--------------|--------------------------|------------|--------------|-------------------|------------|--------------|--------------------------|------------|--------------|
| | Drift ratio | | | Relative rotation of CCB | | | Drift ratio | | | Relative rotation of CCB | | |
| | β_d | p -value | | β_d | p -value | | β_d | p -value | | β_d | p -value | |
| | | vs. M | vs. $\ln(R)$ | | vs. M | vs. $\ln(R)$ | | vs. M | vs. $\ln(R)$ | | vs. M | vs. $\ln(R)$ |
| PGA | 0.59 | 0.32 | 0.57 | 0.28 | 0.28 | 0.61 | 0.49 | 0.35 | 0.59 | 0.20 | 0.33 | 0.62 |
| PGV | 0.59 | 0.04 | 0.32 | 0.25 | 0.04 | 0.33 | 0.48 | 0.03 | 0.59 | 0.17 | 0.04 | 0.58 |
| PGD | 0.71 | 0.09 | 0.01 | 0.45 | 0.07 | 0.01 | 0.6 | 0.07 | 0.02 | 0.32 | 0.08 | 0.02 |
| S_a | 0.62 | 0.26 | 0.81 | 0.31 | 0.25 | 0.8 | 0.51 | 0.33 | 0.81 | 0.19 | 0.32 | 0.85 |

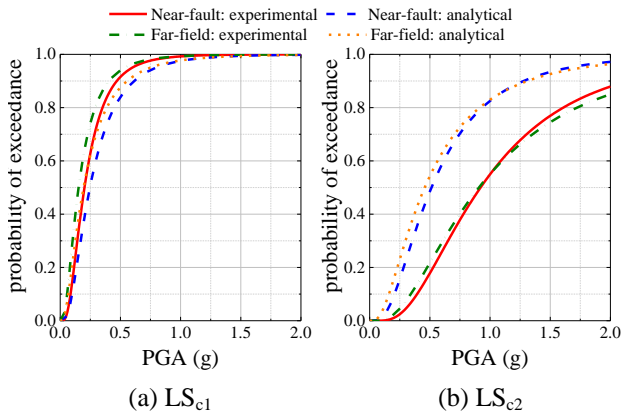


Fig. 12 Component fragility curves in terms of the CCB rotation

In addition, it is observed from Table 7 that the dispersion of the demand (for both the NF and FF ground motions) corresponding to the relative rotation of CCB is smaller than that of drift ratio of piers under four IMs. Therefore, the relative rotation of CCB tends to be a more appropriate EDP than the drift ratio of piers to represent the response of the prototype composite bridge.

5. Seismic fragility analysis

5.1 Seismic fragility curves of bridge components

Based on the aforementioned developed demand and capacity model for the CCB and pier, the component fragility curve can be derived using Eq. (1). The component fragility curves for the CCB are presented in Fig. 12, from which the evident relative difference between the results calculated based on the experimental and the analytical limit states are observed. The relative difference tends to be larger for the limit states with the higher level of damages. The difference between the component fragility of the near-fault and far-field earthquakes for the CCB is limited. This is due to the fact that the short bridge, with a predominate period of 0.6s, is less sensitive to the peak velocity of NF ground motions.

As shown in Fig. 12 (a), the probability of damage occurrence at the CCB is about 50% when the PGA is equal to 0.2g. When the PGA is equal to 0.5g, the probability associated with the damage exceeding the limit state of yielding rotation is about 90%. At the same time, the

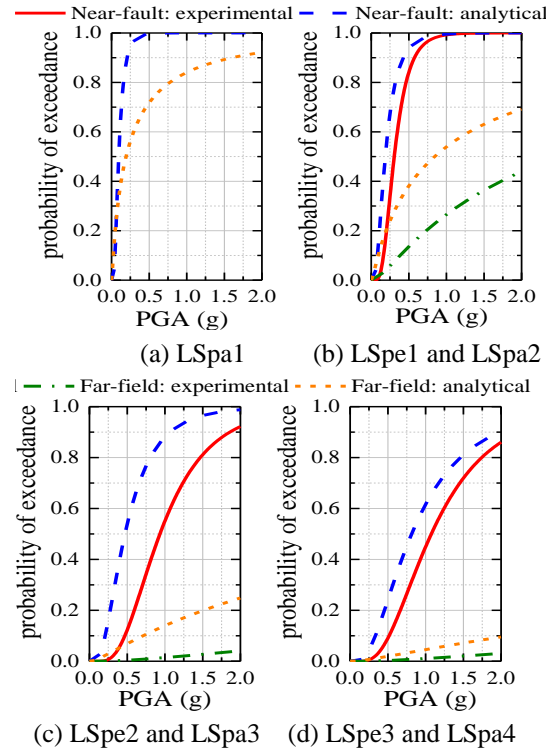


Fig. 13 Component fragility curves at the middle pier in terms of the drift ratio

probability of damage exceeding the ultimate damage state in CCB is about 25% based on test model and 50% based on the analytical model. When the PGA is equal to 1g, the exceedance probability for CCB failure is only about 55% based on the experimental fragility curves. This shows that the CCB joint has good seismic performance even under the NF earthquakes.

Fig. 13 shows the component fragility curves of the middle pier in terms of the drift ratio. It can be seen that the probability of exceedance results by the experimental model are smaller than that by the analytical for both NF and FF ground motions. Moreover, the differences between the experimental fragility and analytical fragility curves are significant. Comparing with the fragility curves of the CCB component, it is observed that the pier is not always the most vulnerable component for this typical composite bridge and the fragility of the CCB should be considered at the same time.

5.2 Seismic fragility curves of bridge system

Table 8 Limit states and EDPs of the bridge system

| LS for bridge | Description of limit states | Repair method | EDP: Relative rotation of CCB | | EDP: Drift ratio of pier | |
|---------------|--|--|-------------------------------|----------------------------|--------------------------|----------------------------|
| | | | Test (from Table 1) | Analysis (from Table 4) | Test (from Table 2) | Analysis (from Table 5) |
| LS0 | Negligible Damage: onset of cracking in the pier | No repair or seal cracks | - | - | - | LS _{pa} 1 |
| LS1 | Limited Damage: onset yielding in the CCB and spalling of concrete cover of the pier | Seal cracks, minor removal in the CCB and patching of concrete | LS _{ce} 1 | LS _{ca} 1 | LS _{pe} 1 | LS _{pa} 2 |
| LS2 | Significant Damage: buckling of steel bars in the pier | Major patching of concrete or reinforcement of the pier | - | - | LS _{pe} 2 | LS _{pa} 3 |
| LS3 | Near-collapse Damage (or Local Failure): failure of CCB and fracture of bars in the pier | Replace half of column; replace the CCB | LS _{ce} 2 | LS _{ca} 2 | LS _{pe} 3 | LS _{pa} 4 |
| LS4 | Collapse Damage | Reconstruction | - | - | - | - |

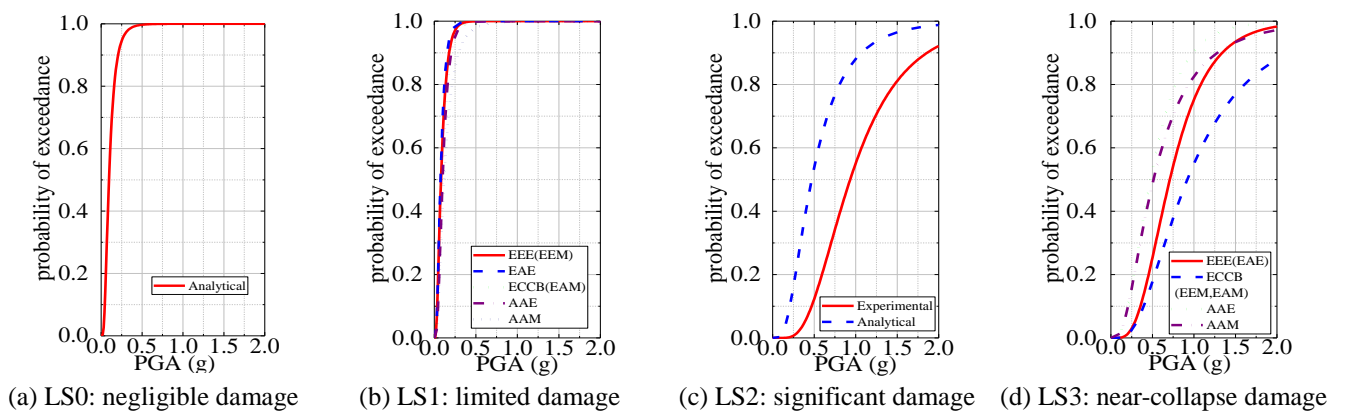


Fig. 16 Comparison of system fragility curves under NF ground motions

The progressive damage states for each bridge component could be considered together to identify the collapse mechanism for the bridge system. According to the damage states observed during the experiment, a total of five limit states are identified and shown in Table 8 for the bridge system based on the selected EDPs, i.e., the relative rotation of the CCB and drift ratio of the pier. In addition, to facilitate the interpretation of the results, the definition of relevant limit states in Eurocode 8-part 3 (2005) has been adopted. The descriptions of the limit states are summarized in Table 8. According to Table 8, damages states from LS0 to LS3 represent the limit states of the CCB and the pier, whereas LS4 represents the total collapse of the bridge. It is also noted that the contribution to LS0 and LS2 are mainly from the pier.

There are two commonly used methods in combining the component fragility curves to derive the system fragility curves. (1) Method I. Based on the conservative assumption of the tandem connection between components (Stefanidou and Kappos 2017), the system fragility can be modeled as

$$P(\text{System Fragility}) = 1 - \prod_{c=1}^n [1 - P(\text{Fragility}_c)] \quad (6)$$

in which n is the number of components considered and c denotes a specific component. In this method, each of component fragility has the same weight and it is denoted as the “equality method”; (2) Method II. For each limit state,

Table 9 Combination of the component fragility curves in generating the system fragility curves

| Combination method | Combination method | Damage states of the CCB | | Damage states of the pier | |
|--------------------|--------------------|-------------------------------------|-------------------------------------|-------------------------------------|-------------------------------------|
| | | Experimental | Analytical | Experimental | Analytical |
| EEE | Equality | <input checked="" type="checkbox"/> | <input type="checkbox"/> | <input checked="" type="checkbox"/> | <input type="checkbox"/> |
| EEM | Maximum | <input checked="" type="checkbox"/> | <input type="checkbox"/> | <input checked="" type="checkbox"/> | <input type="checkbox"/> |
| EAE | Equality | <input checked="" type="checkbox"/> | <input type="checkbox"/> | <input type="checkbox"/> | <input checked="" type="checkbox"/> |
| EAM | Maximum | <input checked="" type="checkbox"/> | <input type="checkbox"/> | <input type="checkbox"/> | <input checked="" type="checkbox"/> |
| AAE | Equality | <input type="checkbox"/> | <input checked="" type="checkbox"/> | <input type="checkbox"/> | <input checked="" type="checkbox"/> |
| AAM | Maximum | <input type="checkbox"/> | <input checked="" type="checkbox"/> | <input type="checkbox"/> | <input checked="" type="checkbox"/> |
| ECCB | No | <input checked="" type="checkbox"/> | <input type="checkbox"/> | <input type="checkbox"/> | <input type="checkbox"/> |

the maximum of the component fragilities is assumed as the system fragility over the given limit state. This method can be expressed as

$$P(\text{System Fragility}) = \max_{c=1}^n [P(\text{Fragility}_c)] \quad (7)$$

This method is denoted as the “maximum method”.

By combining the component fragility curves obtained either analytically or experimentally, a total of seven combinations have been considered and are summarized in Table 9. Specifically, the experimental fragility curves for the CCB are used in approaches of EEE, EEM, EAE, EAM, and ECCB and the experimental fragility curves of the pier are used in approaches of EEE and EEM. Furthermore, the

Table 10 Distribution parameters of mean system fragility for LS1 and LS3

| PGA (g) | Near-fault | | | | Far-field | | | |
|---------|------------|-------|-------|-------|-----------|-------|-------|-------|
| | LS1 | | LS3 | | LS1 | | LS3 | |
| | Mean | SD | Mean | SD | Mean | SD | Mean | SD |
| 0.2 | 0.900 | 0.061 | 0.035 | 0.040 | 0.509 | 0.043 | 0.056 | 0.065 |
| 0.4 | 0.989 | 0.015 | 0.193 | 0.127 | 0.671 | 0.009 | 0.227 | 0.144 |
| 0.6 | 0.998 | 0.004 | 0.394 | 0.163 | 0.754 | 0.003 | 0.366 | 0.164 |
| 0.8 | 0.999 | 0.001 | 0.569 | 0.163 | 0.805 | 0.001 | 0.455 | 0.155 |
| 1 | 1.000 | 0.000 | 0.697 | 0.148 | 0.841 | 0.000 | 0.510 | 0.136 |
| 1.2 | 1.000 | 0.000 | 0.787 | 0.127 | 0.866 | 0.000 | 0.546 | 0.115 |
| 1.4 | 1.000 | 0.000 | 0.848 | 0.106 | 0.885 | 0.000 | 0.572 | 0.096 |
| 1.6 | 1.000 | 0.000 | 0.889 | 0.087 | 0.900 | 0.000 | 0.591 | 0.080 |
| 1.8 | 1.000 | 0.000 | 0.918 | 0.070 | 0.912 | 0.000 | 0.606 | 0.066 |
| 2 | 1.000 | 0.000 | 0.939 | 0.056 | 0.922 | 0.000 | 0.618 | 0.055 |

analytical system fragility curves obtained by the approaches of AAE and AAM are compared with the experimental results.

Fig. 16 presents the system fragility curves of the bridge under NF earthquakes. It was indicated from Fig. 16 (b) and (d) that the probability of exceeding the limit states evaluated according to the approach of ECCB is more conservative than the analytical one, meaning that the analytical fragility may lead to over-conservative results in design or assessment of the bridge.

The distribution parameters of the fragility curves under different seismic intensity levels are reported in Table 10. According to Table 10, the difference between the mean fragility for LS1 under both the NF and FF earthquakes is not large; however, the difference for LS3 becomes more evident. It should be noted that the mean fragility value of the bridge under FF earthquakes is higher than that under the NF earthquakes at the low-intensity levels (i.e., 0.2 g and 0.4 g). However, the bridge is more vulnerable under NF ground motions than FF ground motions under the seismic events with high-intensity levels (equal or greater than 0.6 g). The analysis of results of the standard deviation shows that the uncertainty of the fragility, resulting from the combination approach of component fragility curves, has the largest value at the intensity level of 0.6 g for LS3. Meanwhile, the uncertainties for LS1 show the decreasing trend with the increasing intensity level.

6. Conclusions

This paper studies seismic fragility of a typical steel-concrete composite bridge with the improved deck-to-pier connection joint configuration at CCB. The damage states for both the critical components of the CCB and the pier are identified based on the quasi-static test on a typical steel-concrete composite bridge. The FE model is developed and calibrated to model the damage states of the CCB and bridge pier as observed from the experiment of the test specimen. The component fragility curves for both of the CCB and pier were derived and combined to develop the system fragility curves of the bridge. The following

conclusions can be drawn from this investigation:

1. The seismic fragility of the CCB derived based on experimental model is smaller than that by the analytical model. The relative difference between the experimental and analytical component fragility curves is more than 20% corresponding to the ultimate rotation of the CCB.
2. The relative difference between the experimental and analytical component fragility (in terms of the drift ratio) of the pier is greater than 30% and the appropriate limit states should be identified for the more accurate analysis. The pier is not always the most vulnerable component for the composite bridge and fragility analysis of the CCB should be considered.
3. The system fragility of the bridge shows the large dispersion of 0.2 corresponding to the near-collapse limit state under NF ground motions. Under FF earthquakes, the largest dispersion of system fragility is about 0.15.

Acknowledgments

The research for this paper is supported by the European Project SEQBRI (Performance-Based Earthquake Engineering Analysis of Short-Medium Span Steel-Concrete Composite Bridges) under Grant No. RFSR-CT-2012-00032, the National Science Foundation of China (Grant Nos. 51678209, 51378162), the Ministry of Science and Technology of China (Grant No. 2013BAJ08B01), and the State Key Laboratory for Disaster Reduction in Civil Engineering (Grant No. SLDRCE12-MB-04).

References

- Baker, J.W. (2013), "Efficient analytical fragility function fitting using dynamic structural analysis", *Earthq. Spectra*, **31**(1), 579-599.
- Banerjee, S. and Chi, C. (2013), "State-dependent fragility curves of bridges based on vibration measurements", *Prob. Eng. Mech.*, **33**(10), 116-125.
- Berry, M. and Eberhard, M.O. (2003), "Performance models for flexural damage in reinforced concrete columns", PEER Report 2003/18; Pacific Earthquake Engineering Research Center, College of Engineering, University of California, Berkeley.
- Billah, A.M., Alam, M.S. and Bhuiyan, M.R. (2012), "Fragility analysis of retrofitted multicolumn bridge bent subjected to near-fault and far-field ground motion", *J. Bridge Eng.*, **18**(10), 992-1004.
- Bursi, O.S., Ferrario, F. and Fontanari, V. (2002), "Non-linear analysis of the low-cycle fracture behaviour of isolated tee stub connections", *Comput. Struct.*, **80**(27-30), 2333-2360.
- Celik, O.C. and Ellingwood, B.R. (2010), "Seismic fragilities for non-ductile reinforced concrete frames-role of aleatoric and epistemic uncertainties", *Struct. Saf.*, **32**(1), 1-12.
- CEN (2005), Eurocode 8: Design of Structures for Earthquake Resistance, Part 1: General Rules, Seismic Actions and Rules for Buildings, European Committee for Standardization; Brussels, Belgium.
- CEN (2005), Eurocode 8: Design of Structures for Earthquake Resistance-Part 3: Assessment and Retrofitting of Buildings, European Committee for Standardization; Brussels, Belgium
- CEN (2006), Eurocode 4: Design of Composite Steel and Concrete

- Structures, European Committee for Standardization; Brussels, Belgium.
- Cornell, C.A., Jalayer, F., Hamburger, R.O. and Foutch, D.A. (2002), "Probabilistic basis for 2000 sac federal emergency management agency steel moment frame guidelines", *J. Struct. Eng.*, **128**(4), 526-533.
- ECCS (1986), Recommended Testing Procedure for assessing the Behaviour of Structural Steel Elements under Cyclic Load, ECCS - European Convention for Constructional Steelwork.
- Frankie, T.M. (2013), "Impact of complex system behavior on seismic assessment of RC bridges", Ph.D. Dissertation; University of Illinois at Urbana-Champaign, Illinois.
- Gattesco, N. and Giuriani, E. (1996), "Experimental study on stud shear connectors subjected to cyclic loading", *J. Constr. Steel Res.*, **38**(1), 1-21.
- Han, Q., Zhou, Y., Du, X., Huang, C. and Lee, G.C. (2014), "Experimental and numerical studies on seismic performance of hollow RC bridge columns", *Earthq. Struct.*, **7**(3), 251-269.
- Han, Q., Zhou, Y., Ou, Y. and Du, X. (2017), "Seismic behavior of reinforced concrete sacrificial exterior shear keys of highway bridges", *Eng. Struct.*, **139**, 59-70.
- Ibarra, L.F. (2005), "Global collapse of frame structures under seismic excitations", Ph.D. Dissertation; Stanford University.
- Iman, R.L. (2008), *Latin Hypercube Sampling*, John Wiley & Sons, Ltd.
- Liu, Y., Lu, D.G. and Paolacci, F. (2015), "Multivariate probabilistic seismic demand analysis of steel-concrete composite bridges under near-fault pulse-like ground motions", *International Conference on Multi-Span Large Bridges*, Portugal.
- Liu, Y., Lu, D.G. and Paolacci, F. (2016), "Probabilistic seismic resilience analysis for bridges shocked by near-fault pulse-like ground motions", *Maintenance, Monitoring, Safety, Risk and Resilience of Bridges and Bridge Networks - Proceedings of the Eighth International Conference on Bridge Maintenance, Safety and Management*, Foz do Iguacu, Brazil, June.
- Lu, D.G., Yu, X.H., Jia, M.M. and Wang, G.Y. (2014), "Seismic risk assessment for a reinforced concrete frame designed according to chinese codes", *Struct. Infrastr. Eng.*, **10**(10), 1295-1310.
- Luco, N. and Cornell, C.A. (2007), "Structure-specific scalar intensity measures for near-source and ordinary earthquake ground motions", *Earthq. Spectra*, **23**(2), 357-392.
- Mazzoni, S., McKenna, F., Scott, M.H. and Fenves, G.L. (2006), *OpenSees Command Language Manual*, Pacific Earthquake Engineering Research Center.
- Muntasir Billah, A. and Shahria Alam, M. (2015), "Seismic fragility assessment of highway bridges: A state-of-the-art review", *Struct. Infrastr. Eng.*, **11**(6), 804-832.
- NGA-west2 (2017), NGA-west2 Strong Ground Motion Database; Pacific Earthquake Engineering Research Center, America. <http://peer.berkeley.edu/ngawest2/databases/>.
- Nielson, B.G. (2005), "Analytical fragility curves for highway bridges in moderate seismic zones", Ph.D. Dissertation; Georgia Institute of Technology.
- Padgett, J.E. and Desroches, R. (2008), "Methodology for the development of analytical fragility curves for retrofitted bridges", *Earthq. Eng. Struct. Dyn.*, **37**(8), 1157-1174.
- Paolacci, F., Giannini, R., Malena, M., Slessandri, S. and Paglini, A. (2014), "Toward a performance-based earthquake engineering analysis of short-medium span steel-concrete composite bridges", *Proceedings of the European Conference on Earthquake Engineering*.
- Paolacci, F., Bursi, O.S., Popa, N., Cremona, C., Stathopoulos, S. and Hoffmeister, B. (2016), "Performance-based earthquake engineering analysis of short-medium span steel-concrete composite bridges", RFSR-CT-2012-00032; Roma Tre University.
- Porter, K., Kennedy, R. and Bachman, R. (2007), "Creating fragility functions for performance-based earthquake engineering", *Earthq. Spectra*, **23**(2), 471-489.
- Sengupta, P. and Li, B. (2013), "Modified Bouc-Wen model for hysteresis behavior of RC beam-column joints with limited transverse reinforcement", *Eng. Struct.*, **46**(46), 392-406.
- Sengupta, P. and Li, B. (2014), "Seismic fragility evaluation of lightly reinforced concrete beam-column joints", *J. Earthq. Eng.*, **18**(7), 1102-1128.
- Stefanidou, S.P. and Kappos, A.J. (2017), "Methodology for the development of bridge-specific fragility curves", *Earthq. Eng. Struct. Dyn.*, **46**(1), 73-93.
- Tondini, N. and Stojadinovic, B. (2012), "Probabilistic seismic demand model for curved reinforced concrete bridges", *Bull. Earthq. Eng.*, **10**(5), 1455-1479.
- Tubaldi, E., Barbato, M. and Dall'asta, A. (2010), "Transverse seismic response of continuous steel-concrete composite bridges exhibiting dual load path", *Earthq. Struct.*, **1**(1), 21-41.
- Zhai, C.H., Chang, Z.W., Li, S., Chen, Z.Q. and Xie, L.L. (2013), "Quantitative identification of near-fault pulse-like ground motions based on energy", *Bull. Seismol. Soc. Am.*, **103**(5), 2591-2603.

AT

Appendix

Table 1 The selected NF ground motion records

| Event No. | NGA No. | Station | PGV (cm/s) | PGV/PGA | $S_a(T_1, 5\%)$ (g) | M_w | T_p (s) | E_p |
|-----------|---------|------------------|------------|---------|---------------------|-------|-----------|-------|
| 1 | 161 | H-BRA225 | 35.9 | 0.23 | 0.21 | 6.5 | 3.2 | 0.47 |
| 2 | 170 | H-ECC092 | 68.8 | 0.3 | 0.32 | 6.5 | 3.5 | 0.55 |
| 3 | 171 | H-EMO270 | 90.5 | 0.31 | 0.4 | 6.5 | 2.8 | 0.71 |
| 4 | 171 | H-EMO000 | 71.7 | 0.23 | 0.36 | 6.5 | 2.5 | 0.71 |
| 5 | 173 | H-E10050 | 47.5 | 0.28 | 0.2 | 6.5 | 3.2 | 0.54 |
| 6 | 178 | H-E03140 | 46.8 | 0.21 | 0.28 | 6.5 | 2.6 | 0.66 |
| 7 | 179 | H-E04230 | 76.6 | 0.22 | 0.54 | 6.5 | 3.4 | 0.6 |
| 8 | 181 | H-E06230 | 109.8 | 0.26 | 0.44 | 6.5 | 3.5 | 0.67 |
| 9 | 182 | IMPVALL/H-E07230 | 109.3 | 0.24 | 0.62 | 7.6 | 3.4 | 0.69 |
| 10 | 184 | H-EDA270 | 71.2 | 0.21 | 0.25 | 6.5 | 3.2 | 0.58 |
| 11 | 185 | H-HVP315 | 49.8 | 0.23 | 0.29 | 6.5 | 3.5 | 0.75 |
| 12 | 527 | MVH135 | 40.9 | 0.2 | 0.34 | 6.6 | 2.1 | 0.57 |
| 13 | 1045 | WPI316 | 67.4 | 0.21 | 0.53 | 6.7 | 1.8 | 0.62 |
| 14 | 1148 | KOCAELI/ARC090 | 39.5 | 0.27 | 0.1 | 7.4 | 6.5 | 0.79 |
| 15 | 1148 | ARC090 | 39.5 | 0.27 | 0.1 | 7.4 | 3.6 | 0.64 |
| 16 | 1171 | SKR090 | 79.5 | 0.22 | 0.4 | 7.4 | 6.4 | 0.89 |
| 17 | 1176 | YPT060 | 65.7 | 0.25 | 0.36 | 6.5 | 5 | 0.48 |
| 18 | 1244 | CHY101_N | 115 | 0.27 | 0.7 | 7.6 | 5 | 0.47 |
| 19 | 1244 | CHY101_W | 70.6 | 0.2 | 0.4 | 7.6 | 3.4 | 0.47 |
| 20 | 1462 | TCU-E | 40.5 | 0.23 | 0.31 | 7.6 | 5.8 | 0.48 |
| 21 | 1480 | TCU036_N | 50.2 | 0.39 | 0.24 | 7.6 | 5.8 | 0.6 |
| 22 | 1480 | TCU036_W | 59.6 | 0.44 | 0.23 | 7.6 | 5.9 | 0.6 |
| 23 | 1482 | TCU039_N | 54 | 0.38 | 0.21 | 7.6 | 5.4 | 0.65 |
| 24 | 1482 | TCU039_W | 50 | 0.25 | 0.16 | 7.6 | 8.3 | 0.45 |
| 25 | 1488 | TCU048_N | 48.3 | 0.27 | 0.18 | 7.6 | 7.8 | 0.45 |
| 26 | 1488 | TCU048_W | 32.6 | 0.27 | 0.24 | 7.6 | 11.2 | 0.44 |
| 27 | 1489 | TCU049-N | 61.2 | 0.25 | 0.37 | 7.6 | 5.1 | 0.66 |
| 28 | 1490 | TCU050-W | 36.9 | 0.26 | 0.23 | 7.6 | 9.8 | 0.53 |
| 29 | 1492 | TCU052_N | 118.4 | 0.29 | 1.15 | 7.6 | 10.1 | 0.7 |
| 30 | 1492 | TCU052_W | 159 | 0.47 | 0.96 | 7.6 | 6.8 | 0.64 |
| 31 | 1494 | TCU054_W | 59.4 | 0.41 | 0.29 | 7.6 | 8.2 | 0.63 |
| 32 | 1496 | TCU051_W | 49.3 | 0.27 | 0.29 | 7.6 | 7.7 | 0.35 |
| 33 | 1497 | TCU057_N | 42.6 | 0.47 | 0.16 | 7.6 | 7.6 | 0.5 |
| 34 | 1497 | TCU057_W | 35.2 | 0.3 | 0.2 | 7.6 | 10.3 | 0.52 |
| 35 | 1498 | TCU059_W | 59.4 | 0.37 | 0.41 | 7.6 | 6.6 | 0.49 |
| 36 | 1499 | TCU060-N | 45.3 | 0.44 | 0.23 | 7.6 | 6.8 | 0.52 |
| 37 | 1500 | TCU061_W | 40.3 | 0.29 | 0.24 | 7.6 | 5.6 | 0.41 |
| 38 | 1501 | TCU063_N | 73.1 | 0.56 | 0.28 | 7.6 | 4.2 | 0.48 |
| 39 | 1502 | TCU064_N | 54 | 0.47 | 0.18 | 7.6 | 7.6 | 0.49 |
| 40 | 1502 | TCU064_W | 39.2 | 0.37 | 0.18 | 7.6 | 7.6 | 0.51 |
| 41 | 1510 | TCU075_W | 88.3 | 0.27 | 0.29 | 7.6 | 4 | 0.7 |
| 42 | 1515 | TCU082_N | 40.5 | 0.22 | 0.29 | 7.6 | 7.7 | 0.4 |
| 43 | 1515 | TCU082_W | 58.4 | 0.27 | 0.33 | 7.6 | 8.2 | 0.42 |
| 44 | 1519 | TCU087-N | 37.1 | 0.31 | 0.25 | 7.6 | 4.5 | 0.56 |
| 45 | 1519 | TCU087-W | 40.8 | 0.33 | 0.18 | 7.6 | 8.5 | 0.56 |
| 46 | 1527 | TCU100_N | 46.5 | 0.41 | 0.17 | 7.6 | 7.9 | 0.4 |
| 47 | 1527 | TCU100_W | 34.6 | 0.3 | 0.23 | 7.6 | 11.1 | 0.53 |
| 48 | 1528 | TCU101_N | 49.4 | 0.2 | 0.33 | 7.6 | 5.6 | 0.44 |
| 49 | 1528 | TCU101_W | 67.9 | 0.34 | 0.28 | 7.6 | 6 | 0.59 |
| 50 | 1529 | TCU102_N | 77.1 | 0.47 | 0.57 | 7.6 | 2.9 | 0.4 |
| 51 | 1529 | TCU102_W | 112.4 | 0.38 | 0.66 | 7.6 | 3.7 | 0.47 |
| 52 | 1530 | TCU103_W | 61.9 | 0.47 | 0.36 | 7.6 | 6.7 | 0.59 |
| 53 | 1531 | TCU104_N | 47.2 | 0.57 | 0.18 | 7.6 | 6.7 | 0.49 |

Table 1 Continued

| Event No. | NGA No. | Station | PGV (cm/s) | PGV/PGA | $S_a(T_1, 5\%)$ (g) | M_w | T_p (s) | E_p |
|-----------|---------|----------|--------------|-----------|---------------------|-------|-----------|-------|
| 54 | 1531 | TCU104_W | 36.6 | 0.35 | 0.3 | 7.6 | 7.6 | 0.49 |
| 55 | 1532 | TCU105_W | 34.6 | 0.32 | 0.16 | 7.6 | 5.9 | 0.52 |
| 56 | 1535 | TCU109-W | 50.8 | 0.33 | 0.33 | 7.6 | 6.5 | 0.39 |
| 57 | 1548 | TCU128_N | 68.8 | 0.41 | 0.25 | 7.6 | 4.3 | 0.64 |
| 58 | 1548 | TCU128_W | 73 | 0.54 | 0.28 | 7.6 | 8.1 | 0.64 |
| 59 | 1550 | TCU136_N | 47.5 | 0.27 | 0.44 | 7.6 | 5.1 | 0.56 |
| 60 | 1550 | TCU136_E | 55.8 | 0.29 | 0.43 | 7.6 | 8.4 | 0.56 |